JGR Space Physics

RESEARCH ARTICLE
10.1029/2023JA032051

Key Points:

- The medium-scale traveling ionospheric disturbances (MSTIDs) evolution under stormtime electrodynamic forcing is simulated for the first time
- The effect of stormtime large horizontal density gradients associated with storm-enhanced density (SED) is considered in two-dimensional MSTIDs simulations
- The development of MSTIDs is primarily influenced by storm electric fields and SED-related density gradients

Correspondence to:
J. Lei,
leijh@ustc.edu.cn

Citation:
Wang, X., Lei, J., Zhang, S.-R., Li, Z., Dang, T., Luan, X., & Dou, X. (2024). Simulation of nighttime medium-scale traveling ionospheric disturbances in the midlatitude ionosphere during stormtime. *Journal of Geophysical Research: Space Physics*, *129*, e2023JA032051. https://doi.org/10.1029/2023JA032051

Received 5 SEP 2023
Accepted 20 MAY 2024

Simulation of Nighttime Medium-Scale Traveling Ionospheric Disturbances in the Midlatitude Ionosphere During Stormtime

Xiaochuan Wang[1,2,3], Jiuhou Lei[1], Shun-Rong Zhang[4], Zezhong Li[1], Tong Dang[1], Xiaoli Luan[1], and Xiankang Dou[1]

[1]Deep Space Exploration Laboratory/School of Earth and Space Sciences, University of Science and Technology of China, Hefei, China, [2]CAS Center for Excellence in Comparative Planetology/CAS Key Laboratory of Geospace Environment/Mengcheng National Geophysical Observatory, University of Science and Technology of China, Hefei, China, [3]Collaborative Innovation Center of Astronautical Science and Technology, Harbin, China, [4]Haystack Observatory, Massachusetts Institute of Technology, Westford, MA, USA

Abstract The generation of medium-scale traveling ionospheric disturbances (MSTIDs) in the mid-latitude F region ionosphere, particularly in the presence of sporadic E (Es) layers or geomagnetically conjugate features, has been the focus of extensive investigation using both observational and numerical modeling approaches. Recent observations have revealed the occurrence of nighttime MSTIDs over the continental US during storm conditions even without invoking the Es instability. While this phenomenon is considered to be electrified and likely associated with the Perkins instability, the influences of storm-enhanced density (SED), electric fields, and winds on the excitation of nighttime MSTIDs remain a complicated issue and require further quantitative analysis. In this study, we develop a two-dimensional numerical model of the nighttime ionospheric electrodynamics at midlatitudes using the ionospheric ion continuity equation and the electric field Poisson equation to investigate the characteristics of MSTIDs in the SED base region during storm conditions. We demonstrate that the magnetic inclination effect can explain the lower latitude preference of the MSTIDs during magnetic storms, while the development of MSTIDs is primarily influenced by intense storm electric fields under the background ionospheric condition of large density gradients associated with SED. However, the impact of neutral winds on the MSTIDs growth varies, depending on their specific direction determined by the strongly dynamic spatiotemporal variation of the thermosphere and ionosphere during storms. Therefore, the MSTIDs stormtime scenario results from a combination of multiple important factors.

1. Introduction

Nighttime medium-scale traveling ionospheric disturbances (MSTIDs) have been detected by a variety of observation methods, including Global Positioning System (GPS) Total Electron Content (TEC) observations, all-sky air glow imaging in the midlatitude ionosphere. They are characterized by stratified fluctuations of the electron density with vertical displacements and typically have horizontal wavelengths of 100–500 km with phase speed ranging between 50 and 150 m/s (Kelley, 2011; Shiokawa & Idhara et al., 2003). In the northern Hemisphere, the wave fronts of MSTIDs at night are mainly striped in the direction of northwest to southeast, which are not aligned with the geomagnetic field line, and typically travel westward and toward the equator (Duly et al., 2013; Kotake et al., 2007; Narayanan et al., 2014; Otsuka et al., 2013).

The Perkins instability is suggested to be the possible mechanism to explain the nighttime MSTIDs structures and developments (Perkins, 1973). The external effective electric field $\boldsymbol{E}_0^*$, when being applied to the wavy electron density fluctuations, would induce polarization electric fields in order to maintain the current continuity across the wavefronts with inhomogeneous Pedersen conductivity. If $\boldsymbol{E}_0^*$ direction is northeastward in the northern hemisphere, these electric fields generate upward ion drifts for lower conductivity regions. Perkins (1973) deduced the linear growth rate of the instability pattern in the stable nocturnal mid-latitude F-layer in the presence of a northeast electric field. Hamza (1999) extended the derivation of the Perkins instability to include the neutral wind and gradients in the background density and conductivity. Also, Zhou and Mathews (2006) derived the Perkins instability from physical arguments, noting that $\boldsymbol{E} \times \boldsymbol{B}$ forces raise and lower (in altitude) the bands of electron density. However, the perturbation growth rate derived from the linear theory of the Perkins instability is too small to explain the observation results. Other mechanisms need to be taken into account to yield the rapid

growth of MSTIDs. Coupling to sporadic E (Es) layers have been theoretically explored (Cosgrove et al., 2004; Tsunoda, 2006; Tsunoda & Cosgrove, 2001), which shows that the growth rate of the coupled instability exceeds that of the Perkins instability (Yokoyama et al., 2009; Yokoyama & Hysell, 2010). Meanwhile, the observation of the mirrored conjugacy of the MSTIDs structures and the numerical simulations of the Perkins instability including effect of the conjugate F region suggest that the coupling with the conjugate ionosphere is important in the evolution of MSTIDs (Duly et al., 2014; Otsuka et al., 2004).

Recently, Zhang et al. (2019, 2022) reported stormtime MSTIDs on TEC maps observed with high precision GNSS measurements. They were associated with intense storm-time electric field as measured by Millstone Hill incoherent scatter radar and Super DARN radar. Kelley et al. (2023) further reported the polarized electric fields in SuperDARN data. They indicated that the Perkins instability drove the MSTIDs development during severe geomagnetic storms. Without involving the Es instability, Zhang et al. (2022) suggested the storm time ionospheric electric fields and neutral wind disturbance dynamo electric fields may result in sufficiently large growth rates. Magnetosphere dawn-to-dusk electric fields, mapping to the ionosphere and creating convection cells poleward to auroral latitudes, can be significantly intensified and quickly expand or penetrate into low latitudes; solar wind and interplanetary electric fields (IEFs) can directly penetrate into the ionosphere (Huang, 2019; Jaggi & Wolf, 1973; Kelley et al., 1979; Nishida, 1968). These prompt penetration electric fields (PPEFs) and substantial midlatitude electric fields with a poleward component associated with Sub-auroral Polarization Stream (SAPS) (Foster & Burke, 2002) may be large enough to produce visible MSTIDs via the Perkins instability. Additional electric fields can also arise due to dynamo action from the disturbed neutral winds, with a large equatorward surge and a westward subrotation (Blanc & Richmond, 1980).

Numerical simulation is an important tool to study the development and evolution of MSTIDs. The previous two-dimensional simulation assumed that the integral plasma density between magnetic flux tubes was the same (i.e., there was no horizontal gradient in the integral density). The stormtime ionospheric variation is characterized by large density gradients at mid- and sub-auroral latitudes, including the dynamic evolution of SED (Foster, 1993) and midlatitude ionospheric trough (Shinbori et al., 2018). The SED structure has a large area of enhancement base region and a long and narrow plume extended into dayside high latitudes (Foster et al., 2021). Such gradients may be an important new aspect for the Perkins instability as suggested by Hamza (1999), but have been ignored in previous simulations which focused primarily on geomagnetic quiet conditions. In our simulations, we have considered the integral density in the continuity equation with horizontal gradients. Therefore, these MSTIDs and instability study provide some realistic specification of the ionospheric conditions with density gradients as well as the large electric fields and winds during a magnetic disturbance period.

2. Model and Methods

2.1. Model Description

In this study, a two-dimensional model is employed to investigate MSTIDs. Positive ions consist of O^+ as the major species for the F region. The ion and electron momentum and continuity equations are written as

$$q(\boldsymbol{E}+\boldsymbol{V_i}\times\mathbf{B})+m_i\boldsymbol{g}-\frac{\nabla P_i}{n}+m_i\nu_{in}(\boldsymbol{U}-\boldsymbol{V_i})=0, \tag{1}$$

$$-q(\boldsymbol{E}+\boldsymbol{V_e}\times\boldsymbol{B})+m_e\boldsymbol{g}-\frac{\nabla P_e}{n_e}+m_e\nu_{en}(\boldsymbol{U}-\boldsymbol{V_e})+m_e\nu_{ei}(\boldsymbol{V_i}-\boldsymbol{V_e})=0, \tag{2}$$

$$\frac{\partial n}{\partial t}+\nabla\cdot(n\boldsymbol{V})=0, \tag{3}$$

where q, $\boldsymbol{E}$, $\boldsymbol{B}$, $\boldsymbol{g}$ represent elementary charge, electric field, magnetic field and gravitational acceleration, respectively, $\boldsymbol{V_i}$ and $\boldsymbol{V_e}$ are the velocity of ion and electron, m_i and m_e are the mass of ion and electron, n denotes the plasma number density (electrical neutrality approximation, $n=n_i=n_e$), ν_{in}, ν_{en}, ν_{ei} represent the ion/electron collision frequency with neutrals and electron-ion collision frequency, respectively, and $\boldsymbol{U}$ denotes the neutral wind. The electric field can be written as

$$\boldsymbol{E}=-\nabla\Phi=\boldsymbol{E}_0-\nabla\varphi, \tag{4}$$

where $\Phi = \Phi_0 + \varphi$ is the electric potential, Φ_0 represents the background electric potential and φ denotes the polarization electric potential. $\boldsymbol{E}_0$ is the background electric field. Φ needs to satisfy the following current conservation condition,

$$\nabla \cdot \boldsymbol{J} = \nabla \cdot \left[q\left(\sum_j n_{i,j} \boldsymbol{V}_{i,j} - n_e \boldsymbol{V}_e \right) \right] = 0, \tag{5}$$

where $\boldsymbol{J}$ represents the current. Because the variation of Φ along a field line is small, one can assume the magnetic field lines are equal potential. A set of equations integrating along magnetic field lines can be derived to describe the plasma instability in the mid-latitude F region,

$$\frac{\partial \mathrm{X}}{\partial t} + \frac{g}{\Omega} \cos I \frac{\partial \mathrm{X}}{\partial y} + \frac{z \times \nabla_\perp \Phi}{B} \cdot \nabla_\perp \mathrm{X} = 0, \tag{6}$$

$$\frac{\partial \Sigma}{\partial t} + \left(\frac{z \times \nabla_\perp \Phi}{B} - \frac{z \times \boldsymbol{g}}{\Omega} \right) \cdot \nabla_\perp \Sigma = \frac{e \sin^2 Ig}{\Omega B H_n} \mathrm{X} + \Sigma \frac{\partial \Phi}{\partial y} \frac{\cos I}{B H_n} + U_z \frac{\sin I}{H_n} \Sigma, \tag{7}$$

$$\nabla_\perp \cdot \{ \Sigma \left[\nabla_\perp \Phi + B(z \times \boldsymbol{U}_\perp) \right] \} = \frac{\partial \mathrm{X}}{\partial y} \frac{ge \cos I}{\Omega} - \frac{2Tk_B}{e} \nabla_\perp^2 \Sigma - \frac{\partial \Sigma}{\partial x} \cos I \left(\frac{2Tk_B}{eH_n} + \frac{Mg}{e} \right), \tag{8}$$

where X represents the Slant Total Electron Content (STEC) obtained by integrating the electron density along the magnetic field line, Σ denotes the Pedersen conductivity integrated along the magnetic field line, H_n represents the neutral atmospheric scale height, and they are given by

$$\mathrm{X} = \int n \, dz, \; \Sigma = \int \frac{en\nu_{in}}{\Omega B} \, dz, \; \frac{1}{H_n} = \frac{1}{\nu_{in}} \frac{\partial \nu_{in}}{\partial h}, \tag{9}$$

Ω is ion cyclotron frequency, I denotes the magnetic inclination, T is plasma temperature (isothermal approximation, $T = T_i = T_e$).

Equations 6–8 are solved with a finite difference method in a special Cartesian coordinate because the mid-latitude magnetic field lines point northward and downward with an inclination in the northern hemisphere, where the x and y axes are directed north-upward and eastward perpendicular to the magnetic field line, respectively, and z-axis points along the magnetic field $\boldsymbol{B}$. Figure 1 shows the coordinate and the two-dimensional computational plane of the model. The model covers the inclined plane of 200 km × 120 km at mid-latitude, with a grid spacing of 2 km. Periodic boundary conditions are applied in the x and y direction because the parameters on the x–y plane are integral and they can be mapped to the horizontal plane. As the addition of gradient destroys the applicable condition of periodic boundary, period-like boundary conditions are introduced, which make the simulated region at the boundary extend outward according to gradient.

The first-order form of Equations 6–8 contain the background terms and the disturbance terms of the three variables X,Σ and Φ. Given the initial equilibrium ionospheric parameters and small perturbations imposed on Σ, the initial electric potential Φ_0 and the polarization electric potential φ can be obtained from Equation 8 by solving the elliptic equation. The electric field $\boldsymbol{E}$ can be calculated simultaneously from Equation 4. Then, through the effect of polarization electric field, the initial perturbations occur in X. The second order van-Leer scheme is used to solve Equations 6 and 7 (Van Leer, 1977).

2.2. Ionospheric Equilibrium State Conditions

The model needs to input initial equilibrium ionospheric parameters and we describe the configuration of these parameters in this section. Miller (1996) and Zhou (2004) showed that the equilibrium state with the presence of neutral wind can be expressed as

$$\frac{e \sin^2 Ig}{\Omega B} \mathrm{X}_0 - \Sigma_0 \frac{E_{0y} \cos I}{B} + U_z \sin I \Sigma_0 = 0. \tag{10}$$

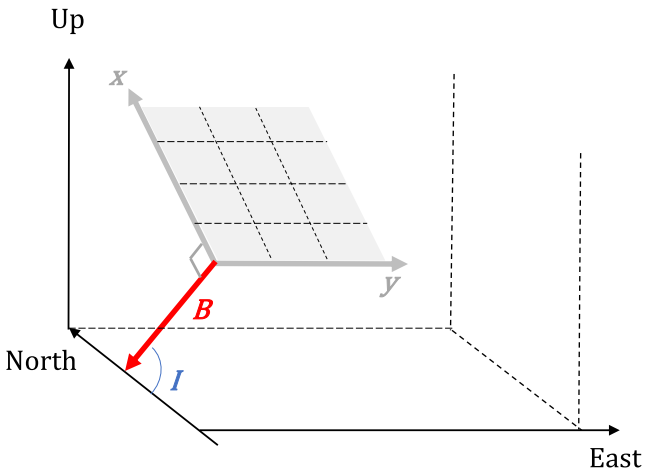

Figure 1. Coordinates and the two-dimensional computational plane of the model.

The initial integral plasma density (or TEC) with a value of about 3.3 TECu used in the model is obtained by integrating the empirical formula of the ionospheric plasma density profile which is a Chapman layer similar to that in the work of Li et al. (2021). X_0 is the slant TEC related to I. The horizontal variation of integral density (dX_h) across the whole calculation plane is defined as

$$dX_h = \frac{X_{0,\max} - X_{0,\min}}{X_{0,\min}} \times 100\%. \quad (11)$$

In our calculation, the horizontal density variation is set as 1.9% for quiet time condition, while for the stormtime MSTIDs simulation, the TEC is changed to 20 TECu and dX_h is changed to 3.9% according to Zhang et al. (2022).

2.3. Parameter Settings

The seeding perturbation induces oscillatory motion of the plasma layer along the magnetic field lines, resulting in variations in the integrated Pedersen conductivity. In the following simulation experiment, a cosine-shaped perturbation $\delta\Sigma$ is introduced to the equilibrium conductivity plane at the onset. The specific form of the initial perturbation is described as follows:

$$\Sigma = \Sigma_0 + \delta\Sigma = \Sigma_0 + \Sigma_0 a_0 \cos(k_x x + k_y y), \quad (12)$$

where the initial perturbation $\delta\Sigma$ is characterized by an amplitude of $a_0 = 0.05$. The wavenumber $k_x = 2\pi/100\ \mathrm{km}^{-1}$ and $k_y = 2\pi/60\ \mathrm{km}^{-1}$ represent the spatial frequencies in the x and y directions, respectively. Equation 6 shows that the change of integrated plasma density X over time is influenced by the coupling of its own horizontal gradient with the gravitational field and the polarization electric field. Therefore, the initial perturbation in Σ can influences X through the polarization electric field when the horizontal gradient in X is considered.

A series of numerical experiments were performed for investigating the effects of ionospheric conditions on the development of MSTIDs. We first ran the controlled experiments (Case 1—Case 4) with electric fields and neutral winds during the magnetically quiet time to verify whether the development of MSTIDs reproduced by this model through Perkins instability consists with prior theoretical expectations. Then, we conducted other controlled experiments (Case 4—Case 7) to study the impact of magnetic inclination on MSTIDs growth. Case 8 utilized a strong electric field decreasing with time, ionospheric plasma density and magnetic inclination $I = 45^\circ$ consists with the observation during magnetic storm time (07/08 September 2017) reported in Zhang et al. (2022). Case 9 applied the same plasma density and magnetic inclination but with a complex wind and a weaker electric field similar to another observation (26 August 2018) reported in Zhang et al. (2022). Table 1 shows the configuration of Case 1—Case 7.

3. Numerical Results

3.1. Effects of Electric Field, Neutral Winds and Magnetic Inclination

Figure 2 illustrates the spatial distribution of the integrated plasma density and the corresponding percentage change of the perturbation in the x–y plane over a simulation period of 3,600 s in Case 1. And the results are presented at 1,200 s intervals. Notably, the structures exhibit a distinct pattern with a northwest-southeast orientation, which gradually develops and propagates in a southwestward direction as time progresses. The maximum amplitude of increase reaches 0.2% in density and 40% in conductivity (not shown) at $t = 3{,}600$ s.

Figure 3 showcases the integrated Pedersen conductivity and the corresponding polarization electric field in the x–y plane at the same time, revealing a similar structural pattern to that observed in the plasma density. The polarization electric field is directed toward the northeastward (southwestward) within the simulation plane, while the $\boldsymbol{E} \times \boldsymbol{B}$ ion velocity points toward the northwestward (southeastward), corresponding to the density or conductivity decrease (increase) fronts (see arrows in Figure 3a).

Table 1
The Ionospheric Environmental Parameters in Case 1—Case 7

	X-Direction electric field E_x	*Y*-Direction electric field E_y	Electric field E_0	*X*-Direction wind field U_x	*Y*-Direction wind field U_y	Perpendicular wind field U_{perp}	*Z*-Direction wind field U_z	Magnetic inclination *I*
Case 1	4.8 mV/m	2.8 mV/m	5.6 mV/m	0	0	0	0	35°
Case 2	4.8 mV/m	2.8 mV/m	5.6 mV/m	**−50 m/s**	70 **m/s**	86 **m/s**	0	35°
Case 3	4.8 mV/m	2.8 mV/m	5.6 mV/m	0	0	0	**−30 m/s**	35°
Case 4	9.6 **mV/m**	5.6 **mV/m**	11.2 **mV/m**	0	0	0	0	35°
Case 5	9.6 mV/m	5.6 mV/m	11.2 mV/m	0	0	0	0	25°
Case 6	9.6 mV/m	5.6 mV/m	11.2 mV/m	0	0	0	0	45°
Case 7	9.6 mV/m	5.6 mV/m	11.2 mV/m	0	0	0	0	55°

To quantify the rate of growth, we utilize the maximum percentage change in the integrated plasma density *X* compared to the initial stationary density X_0. Figure 4 illustrates the maximum variation of *X* over time in Cases 1 to 4. In contrast to Case 1, in which no additional external influences are applied, Case 2 introduces a perpendicular neutral wind $\boldsymbol{U_{perp}}$ of 86 m/s toward the southeast (primarily eastward), which products a northeastward $\boldsymbol{U_{SE}^* \times B}$ effective electric field favorable for Perkins instability. This leads to a significantly accelerated growth rate, as seen in Figure 4, where the blue solid line surpasses the black solid line at corresponding time points. Conversely, in Case 3, the presence of a neutral wind $\boldsymbol{U_z}$ of –30 m/s antiparallel to the magnetic field $\boldsymbol{B}$ (which will not produce the wind dynamo action) retards the growth of the seed perturbation. In Case 4, a doubled electric field contributes to the perturbation development, albeit at a slightly slower phase speed compared to Case 2.

We further investigate the influence of the magnetic inclination for the given electric field $\boldsymbol{E_0}$ = 11.2 mV/m. As shown in Figure 5, a smaller magnetic inclination leads to a more rapid growth of the seed perturbation (Case 5), while an increase in the magnetic inclination causes the perturbation to grow progressively slower (Case 6, and 7). These results are consistent with the observations of Otsuka et al. (2013), who reported a higher occurrence rate of

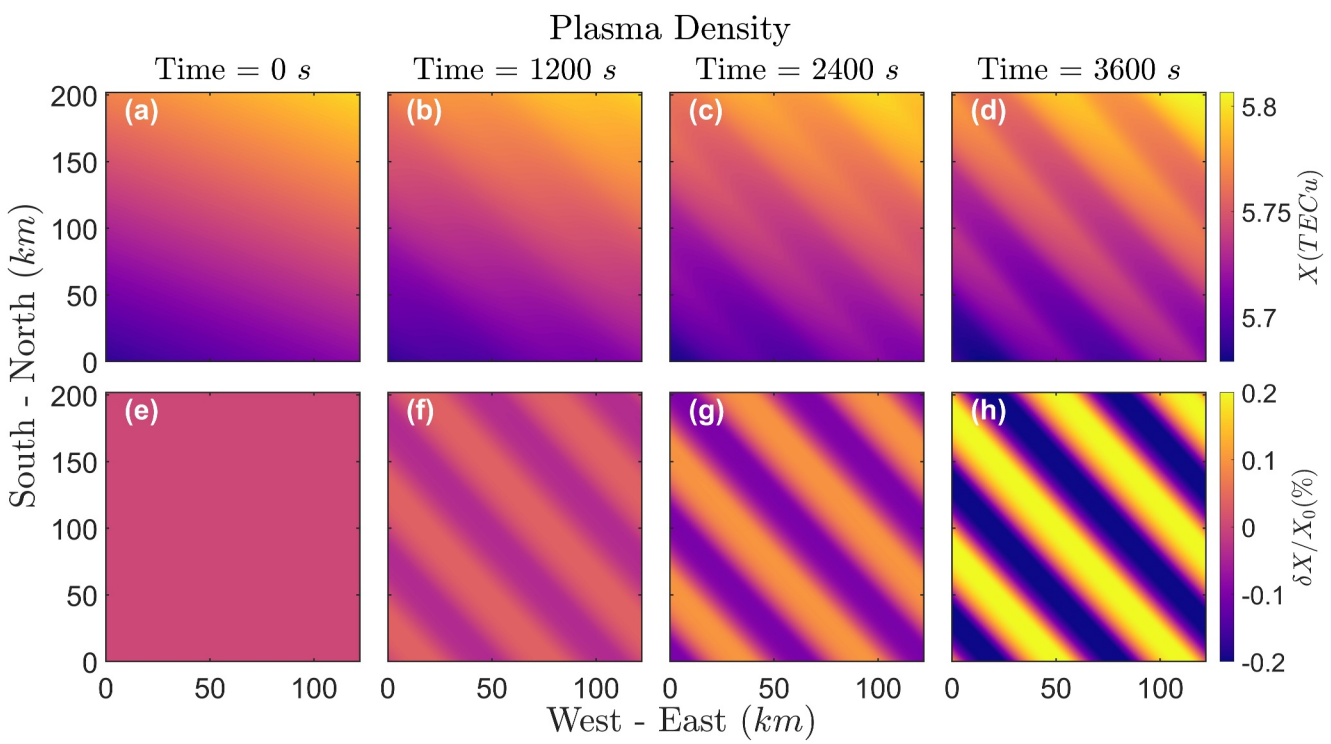

Figure 2. Integrated plasma density (a, b, c, d) and the percentage change (e, f, g, h) with respect to the initial plasma density at *Time* = 0, 1,200, 2,400 and 3600 s in Case 1.

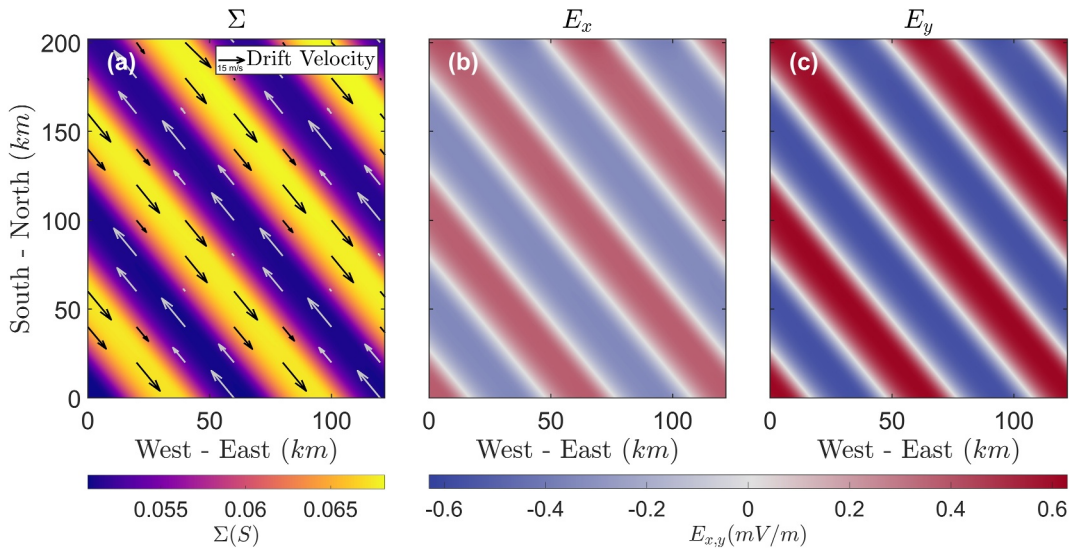

Figure 3. (a) Integrated Pedersen conductivity and the velocity of ion drift (arrows) contributed by the polarization electric field in poleward (b) and eastward (c) directions perpendicular to ***B*** at Time = 2,400 s.

nighttime MSTIDs at lower latitudes compared to higher latitudes, both on a monthly and hourly basis. This magnetic inclination dependence in the evolution of MSTIDs can be partially responsible for the latitudinal difference of the MSTIDs occurrence rate.

3.2. The Effects of Electric Field and Neutral Winds During Magnetic Storm Period

In a recent study by Zhang et al. (2022), the analysis of MSTIDs in the dusk-midnight sector during four geomagnetic storms was conducted using high-resolution Global Navigation Satellite System (GNSS) Total Electron Content (TEC) data. The findings suggested that during intense storm periods, electric fields with a poleward component and enhanced westward winds in the thermosphere can drive the Perkins instability in the F region, even in the absence of sporadic-E layers. These electrified MSTIDs propagate westward, coinciding with

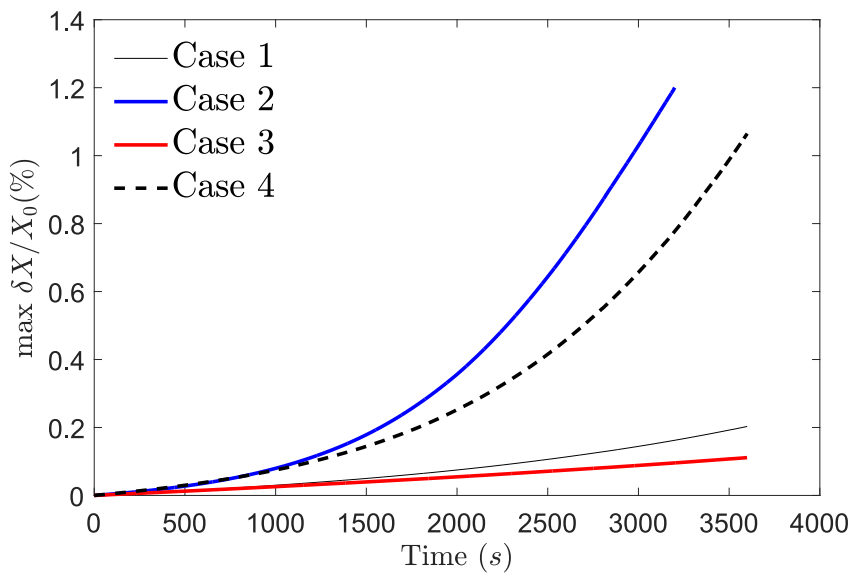

Figure 4. Simulation of geomagnetic quiet-time scenarios. The maximum variation of *X* as a function of time in Case 1 (control group), Case 2 (added perpendicular wind field compared to control group), Case 3 (added wind field antiparallel to ***B*** compared to control group) and Case 4 (doubled the electric field strength compared to control group).

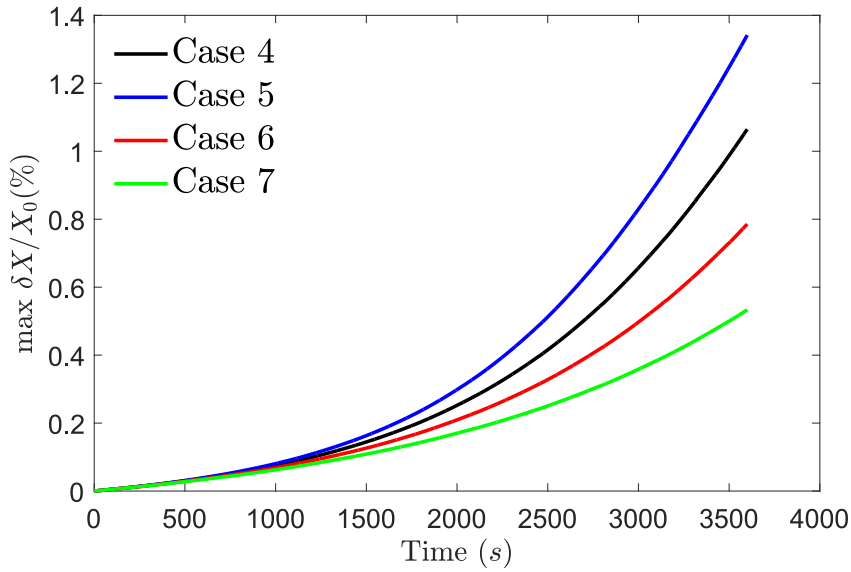

Figure 5. Simulation of dip angle effects. The maximum variation of X as a function of time in Case 4 ($I = 35^{\circ}$), Case 5 ($I = 25^{\circ}$), Case 6 ($I = 45^{\circ}$) and Case 7 ($I = 55^{\circ}$).

the background westward ion flow resulting from disturbance westward wind dynamo and/or Sub-Auroral Polarization Streams (SAPS).

Case 8 introduces a specification of electric field which are similar to storm electric field during a strong magnetic storm event (07/08 September 2017, shown in Figure 6). The most active period of MSTIDs was between 23:00 and 03:00 UT (or between 18:00 and 22:00 LT) as also light-gray shaded area in Figure 6 when IEF Ey was substantially elevated during the main phase and the early recovery phase of the storm.

Figure 7 illustrates the maximum variation of X and the time-varying electric field introduced in Case 8. Note that the ionospheric electric field is about 10% of IEF around the equatorial region (Huang et al., 2005); however, the ionospheric electric field at high latitude, especially in the SAPS region, can have a similar intensity of IEF (Zhang et al., 2022). Thus, we set evolution of electric field in Case 8 as follows. Initially, the electric field starts from a small value of 3 mV/m and is oriented northeastward at an angle of 60° to the eastward direction. It reaches its maximum value of 30 mV/m at $t = 900$ s and subsequently decreases to 20 mV/m and 10 mV/m at $t = 1{,}800$ s and $t = 2{,}700$ s, respectively (indicated by the black solid line). In contrast, we maintain a constant high-value electric field equivalent to the last simulation period at $t = 1{,}800$ s and $t = 2{,}700$ s, represented by the blue and red solid lines in Figure 7a, respectively. The simulation period from $t = 0$–900 s represents the magnetic quiet period before the onset of the magnetic storm, where the electric field remains a small value and the disturbance grows slowly. At $t = 900$ s, the occurrence of the magnetic storm is simulated. As the equivalent electric field increases abruptly, the disturbance experiences accelerated growth, which subsequently slows down as the electric field gradually decreases. Our simulation results align with the observations during the storm period on September 7–8, 2017 (Zhang et al., 2022).

Case 9 includes an additional specification of the winds which were available during another geomagnetic storm (26 August 2018). Figure 8 is the Millstone Hill FPI equatorward and eastward winds during this night. These winds data indicated the equatorward wind surge with 300 m/s maximum speed around 05:00–06:00 UT (or 00:00–01:00 LT) was likely caused by auroral heating. The westward wind surge by ∼200 m/s was even more dramatic for more than ∼5 hr between 01:00 and 06:00 UT (or between 20:00 and 01:00 LT). Furthermore, increased ionospheric plasma density and steep horizontal gradients are incorporated into the simulations in Case 8 and Case 9 to better simulate the ionospheric conditions observed during storms.

The results of Case 9 are presented in Figure 9, illustrating the maximum variation of Σ,X and the variations in the wind field. In this particular simulation, the electric field has a magnitude of 15.1 mV/m, which is weaker compared to Case 8. Throughout the entire simulation period, a significant westward wind with a speed of 200 m/s persists, while a poleward wind of 50 m/s transitions to equatorward, reaching a speed of 150 m/s at $t = 900$ s and

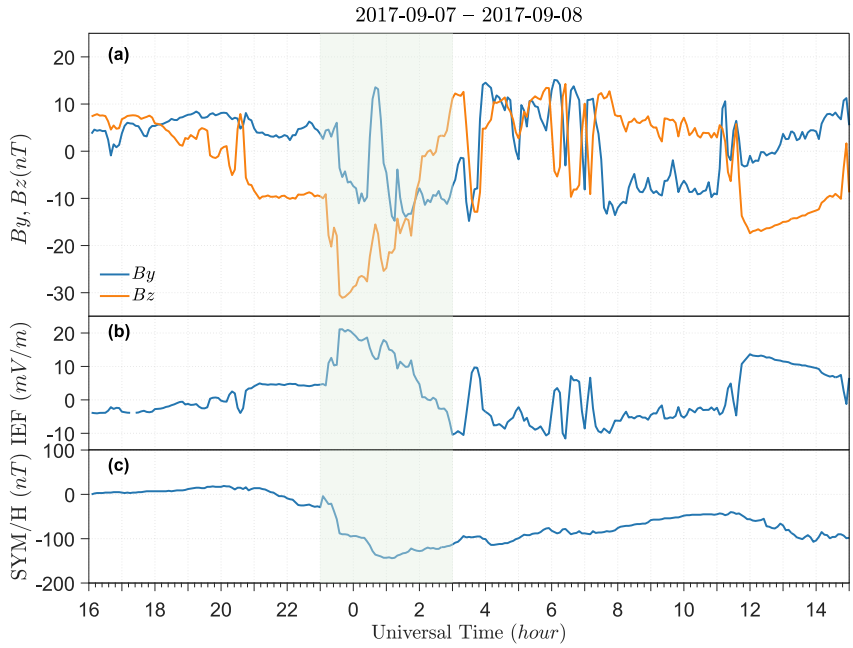

Figure 6. Solar and geomagnetic conditions during 2017-09-07/08. (a) Interplanetary magnetic field components in B_y and B_z; (b) Interplanetary electric field components E_y; (c) SYM-H index. The light-green shaded area is when medium-scale traveling ionospheric disturbances were observed in the continental US according to Figure 3 in Zhang et al. (2022).

accelerating further to 300 m/s at $t = 1{,}800$ s. The perturbations with small amplitude gradually emerge above the integrated plasma density and exhibit slow growth over time. However, there is minimal change observed in the perturbation of the integrated conductivity, and the overall disturbance even diminishes as the wind field veers southward.

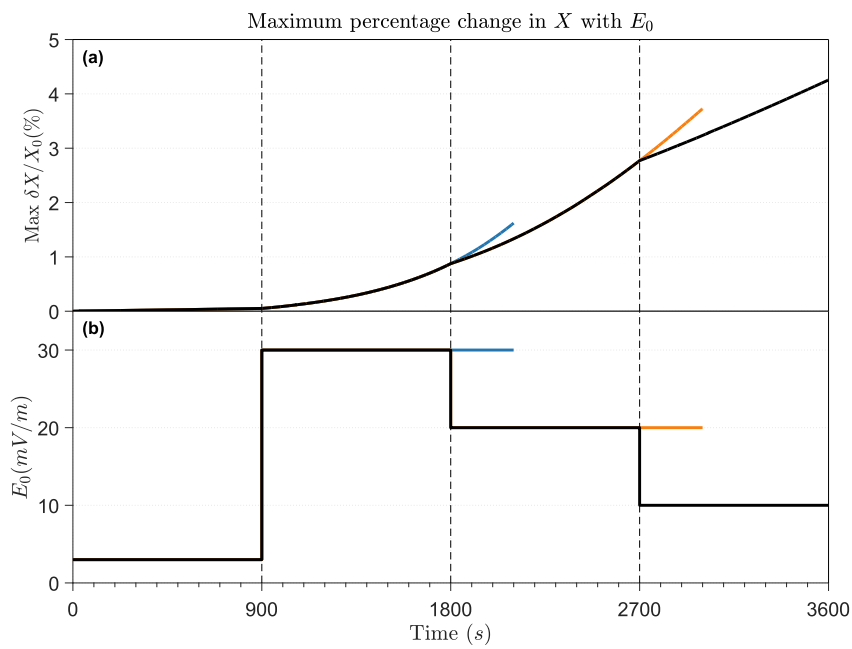

Figure 7. The results and conditions in Case 8 with stormtime density gradients and electric field intensification. (a) The maximum variation of X; (b) Electric filed E_0 used in this simulation.

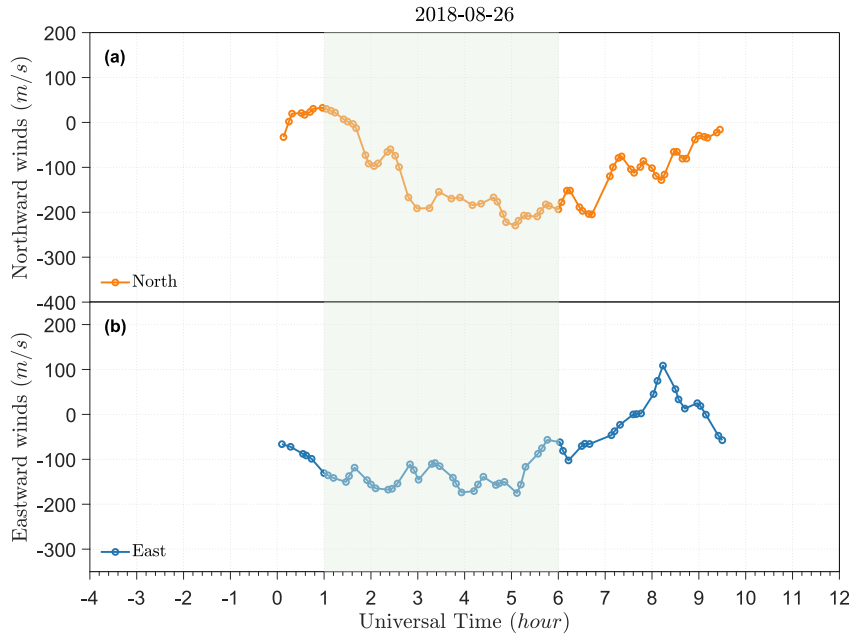

Figure 8. Wind fields observations during storm period. Panels (a) and (b) show Millstone Hill FPI red-line northward and eastward winds at 2018-08-26. The shaded area is when medium-scale traveling ionospheric disturbances were observed in the continental US according to Figure 6 in Zhang et al. (2022).

4. Discussion

In this section, we further discuss the results obtained from the two-dimensional numerical simulation of MSTIDs in the F region. In Case 1, where the electric field is directed northeastward, consistent with Perkins's predicted direction (Perkins, 1973), our results demonstrate that the Perkins instability can self-consistently generate small perturbations in conductivity within the model. In the presence of a horizontal gradient in plasma density, the polarization electric field enhances the vertical oscillations of plasma along the magnetic field lines through the

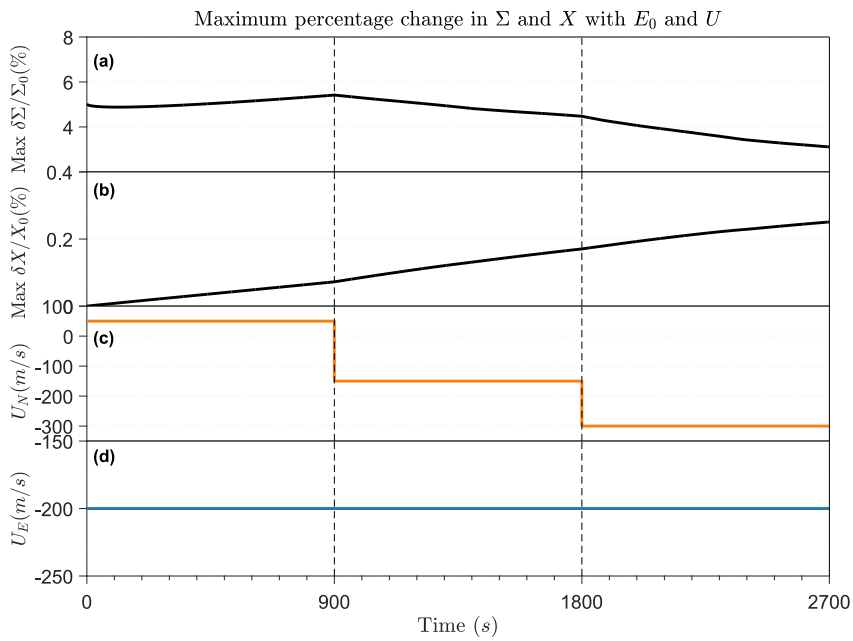

Figure 9. The results and conditions in Case 9. (a) The maximum variation of Σ; (b) The maximum variation of X; (c) Northward wind $\boldsymbol{U_N}$ applied in this simulation; (d) Eastward wind $\boldsymbol{U_E}$ applied in this simulation.

$\boldsymbol{E} \times \boldsymbol{B}$ drift mechanism, resulting in visible patterns in the density plane. According to Equation 6, after the ionospheric equilibrium is reached, disturbances can propagate through the polarization electric field $\nabla_{\perp}\Phi$, inducing density perturbations when the background density gradient $\nabla_{\perp}X$ is non-zero, that is, through a nonlinear process. The result could differ from two-dimensional simulations lacking horizontal gradients, where fringes are only observed in the conductivity plane. It is important to note that the simulation results for Case 1 (Figure 2h) indicate that the maximum amplitude of the density disturbance reaches only 0.2% at $t = 3{,}600$ s. Similarly, the maximum amplitude of the polarization electric field in Figures 3b and 3c is approximately 0.6 mV/m. These magnitudes are considerably smaller than that expected on the basis of observations (Shiokawa & Otsuka et al., 2003). The present results confirm the production of the observed MSTIDs cannot be attributed to the Perkins instability process alone. Chou et al. (2018) demonstrate that the CGW perturbations comprising both ionospheric E and F regions could affect the ionospheric electrodynamics, leading to MSTIDs through wind dynamo. Therefore, electrodynamic processes, including the Es instability, and their coupling with gravity waves in the thermosphere were needed to be consistent with the observation results under geomagnetic quiet conditions.

In Case 2, a rapid increase in the maximum variation of disturbance in X occurs when a southeastward wind $\boldsymbol{U}^{*}_{\boldsymbol{SE}}$ perpendicular to the $\boldsymbol{B}$ is introduced. According to Perkins instability, a northeastward electric field in the Northern Hemisphere is conducive to the development of instability with wave vector pointing southwestward. The equivalent electric field generated by the wind $\boldsymbol{U}^{*}_{\boldsymbol{SE}} \times \boldsymbol{B}$ points to the northeast, which is the favorable direction for Perkins instability. Conversely, in Case 3, when a wind antiparallel to the magnetic field ($\boldsymbol{U}_z$) with an equatorward component is included, the growth of disturbances in the model is slower compared to Case 1. This result is consistent with the predicted growth rate of Perkins instability (Zhou & Mathews, 2006). This is foreseeable because equatorward meridional wind pushes plasma to the higher altitudes where the Pedersen conductivity is expected to decrease in the F region (Narayanan et al., 2018).

Moreover, the results of Case 4—Case 7 indicate that smaller magnetic inclination leads to faster perturbation growth rates under constant electric field conditions. According to the equilibrium Equation 10, changing the magnetic inclination under constant electric field conditions will alter the equilibrium-state integrated conductivity. This implies that the electron density weighted field-line integrated ion-neutral collision frequency $\langle \nu_{in} \rangle$ changes, that is, $\langle \nu_{in} \rangle = \frac{\int n\nu_{in}\, dz}{\int n\, dz}$, corresponding to variations in the F-layer height. The seeding perturbations responsible for generating MSTIDs originate from a diverse range of sources. The abundant energy activity in the high latitude region transmits a large number of the equatorward propagating LSTIDs with zonal wavefronts, which may lead to MSTIDs through coupling the processes being associated with SAPS at mid- and subauroral latitudes. During their continuous evolution and propagation, MSTIDs became much more evident at lower midlatitudes (Kelley et al., 2023; Zhang et al., 2019, 2022). We note that the magnetic field configuration in the mid-latitude region is particularly conducive to the development of those seeding perturbations because during their equatorward propagation, the magnetic field configuration changes persistently with the magnetic inclination decreasing. The higher incidence of MSTIDs observed in middle and low latitudes is also consistent with this result (Otsuka et al., 2013).

To examine the linear development stage of MSTIDs, according to the Perkins instability theory, sinusoidal perturbations ($k_x = 2\pi/100\ \mathrm{km}^{-1}$, $k_y = 2\pi/60\ \mathrm{km}^{-1}$) with a 5% amplitude were utilized under conditions of varying electric fields, winds, and magnetic inclinations. Figure 10 illustrates the theoretical variations of the growth rate of disturbances with different magnitudes of electric fields at $\theta = 60^{\circ}$, and the growth rate variations with or without horizontal gradients. Note that theoretical growth rate is calculated from the formula given in Hamza (1999) and Zhou and Mathews (2006), and the growth rate is rewritten as follows:

$$\gamma = \frac{\cos I}{BH_n}\left[-E_{0y} + \frac{k_y}{k^2}\boldsymbol{k} \cdot (\boldsymbol{E}_0 + \boldsymbol{U}_{\perp} \times \boldsymbol{B})\right] + \frac{\sin I}{H_n}U_z. \tag{13}$$

where $\boldsymbol{k}$ is the wave vector and k represents its magnitude. Using the parameters shown in Table 1, the theoretical growth rates for Cases 2 and 3 are $1.40 \times 10^{-3} s^{-1}$ and $2.35 \times 10^{-4} s^{-1}$, respectively. And the growth rates obtained from the model results are $1.30 \times 10^{-3} s^{-1}$ and $1.73 \times 10^{-4}\, s^{-1}$ for Cases 2 and 3, respectively. Figure 11 is similar to Figure 10 but as a function of magnetic inclinations according to Cases 4–7. All model results are derived from the results of the linear development stage of disturbances. The disturbances in simulations in Figures 10 and 11 develop in a manner largely consistent with Perkins' theory (Perkins, 1973), although there are still a little

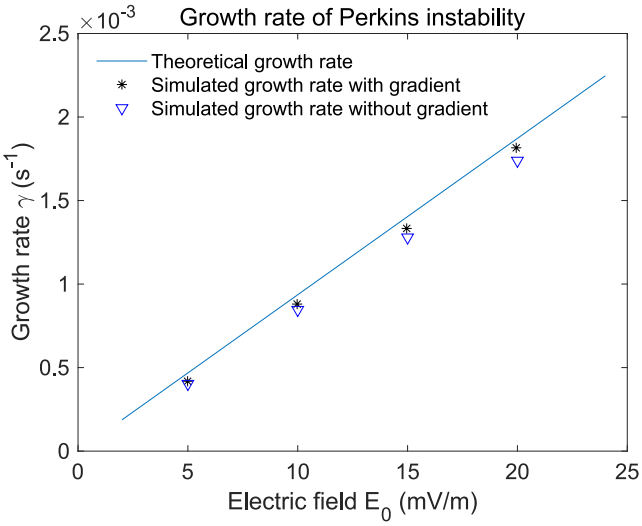

Figure 10. The linear growth rate as a function of the electric fields. Solid line indicates the growth rate according to Perkins' theory. The symbols (*, ∇) denote the growth rate calculated based on model results with or without horizontal gradients.

difference between the simulated and theoretical values. The inclusion of horizontal gradients slightly increases the growth rate of disturbances, which is a kind of gradient drift instability. As the electric field increases or the magnetic inclination decreases, the enhancement of growth rate becomes more pronounced. The results obtained from Case 1—Case 7 within this theoretical solution model once again demonstrate that the perturbation growth rate predicted by Perkins instability theory is insufficient when considering only the background conditions of the ionospheric F layer during the magnetically quiet period. Nevertheless, during magnetic storms, the ionospheric electric field can experience significant amplification, which may be intense enough to trigger the Perkins instability with a sufficiently large linear growth rate. Observations indicate that zonal ion drift speeds can surge up to 1,000 m/s during these periods (Zhang et al., 2017). Similar abrupt surge in the electric field can be attributed to several factors. Firstly, when the magnetospheric convection is enhanced following a southward turning of the interplanetary magnetic field (IMF), high-latitude ionospheric electric fields penetrate toward the low-latitudes, subsequently generating an eastward interplanetary penetrating electric field within the ionosphere (Huang, 2019; Nishioka et al., 2009). Secondly, electric fields associated with SAPS exhibit a pronounced polar component and can persist for over 30 minutes (Erickson et al., 2011; Foster & Burke, 2002). Consequently, the northeast direction emerges as the most plausible vector for the sudden intensification of the ionospheric electric field during a magnetic storm.

In Case 8, we recurrence the observed scenario during storm time, which potentially enhance the growth rate of Perkins instability. When the simulated electric field is artificially amplified (Figure 7b), the growth of small perturbation is obviously accelerated. The disturbance intensity has exceeded 4% at t = 3,400 s, which is equivalent to the TEC variation amplitude often observed by GNSS receivers. It is worth noting that even though we also increase the simulated electric field in Case 4 (with smaller density gradients), the disturbance amplitude only reaches 1.2%, which is smaller than that of the magnetic storm event simulation. According to Equation 6, this difference between Cases 8 and 4 can be attributed to the increased plasma density and horizontal gradient. Furthermore, observational evidence indicates that MSTIDs are typically located near the SED base region, characterized by a substantial density gradient (Zhang et al., 2022). Regardless of whether the electric field maintains a high value over an extended period or decreases over time, the results consistently emphasize the decisive role played by the electric field in the development of MSTIDs during storm time. As shown in Figure 12, the changes in integrated conductivity in Case 8 provide a more intuitive representation of the model's nonlinear processes. At Time = 2,760 s, stripes appear and become more pronounced with distortion after 400 s. The larger growth rate associated with storm-enhanced electric fields in Case 8 leads to the perturbations with the nonlinear behavior. However, secondary perturbations might not emerge within such a short timeframe. Further investigation is required to fully understand its nonlinear behavior.

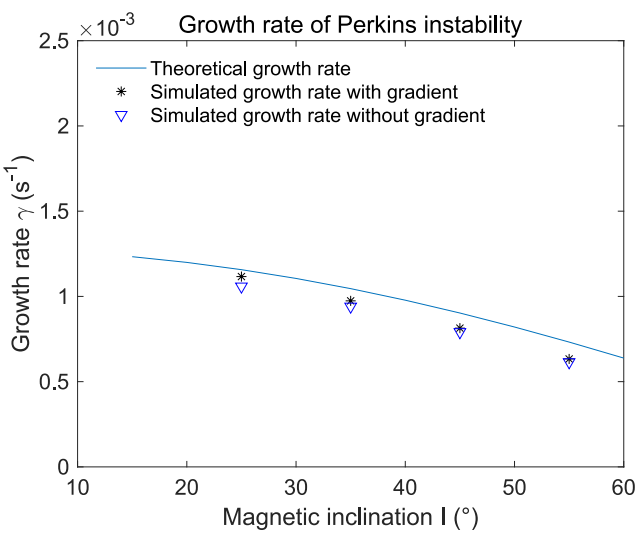

Figure 11. Similar to Figure 10 but as a function of magnetic inclinations according to Cases 4–7.

It is very important to note that Case 9 used a modest electric field value. In more severe magnetic storm events, the electric field magnitude could be even greater. The growth of the disturbance exhibits a distinct difference compared to all previous Cases. The amplitude of density disturbance increases very slowly, and the conductivity disturbance, which started with an 5% initial perturbation amplitude, even dissipates. This discrepancy can be attributed to the stringent constraints imposed by Perkins instability theory on the direction of the effective electric field $\boldsymbol{E}^* = \boldsymbol{E}_0 + \boldsymbol{U} \times \boldsymbol{B}$. The observed strong winds in westward will cause $\boldsymbol{U}_w \times \boldsymbol{B}$ with southward component, which is against Perkins instability growth. For the meridional winds, however, the scenario for the southward direction in the Northern Hemisphere in x–z plane is shown in

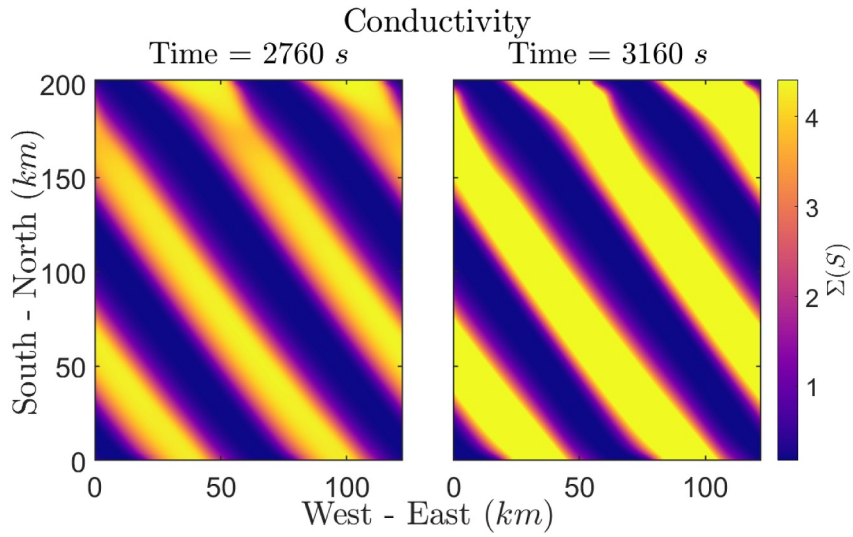

Figure 12. Integrated conductivity in Case 8 at Time = 2,760 s and 3,160 s.

Figure 13. The component $\boldsymbol{U}_S^*$ (perpendicular to $\boldsymbol{B}$) will cause $\boldsymbol{U}_S^* \times \boldsymbol{B}$ with eastward component, which is in favor of Perkins instability, but the other component, anti-parallel to $\boldsymbol{B}$, is against Perkins instability growth (see the results of Case 3). Therefore, the influence of meridional wind on disturbance growth is regulated by magnetic inclination and the magnitude of $\boldsymbol{B}$. Perkins theory necessitates the wave vector to lie between the northeastward (the direction of effective electric field) and the eastward geographic direction in the Northern Hemisphere in Perkins coordinates. The prevailing wind direction in the observation and simulation is southwestward, which provides a southwestward component $\boldsymbol{U}_{sw}^*$ perpendicular to $\boldsymbol{B}$ and a component anti-parallel to $\boldsymbol{B}$. The wind $\boldsymbol{U}_{sw}^* \times \boldsymbol{B}$ alters the direction of the effective electric field $\boldsymbol{E}^*$ to southeastward (unfavorable direction for the southwestward wave vector, which is used in our simulation.) and the antiparallel component also is against the Perkins instability growth. Thus, both components lead to the dissipation of the conductivity disturbance in Case 9. The initial integral density profile in Case 9 exhibits a smooth distribution with a certain horizontal gradient. The well-structured perturbations have leaded to organized polarization electric fields $\boldsymbol{E}_p$. The density perturbation arises and evolves due to the diverse plasma flow driven by the polarization electric field $\boldsymbol{E}_p \times \boldsymbol{B}$ (Figure 9b).

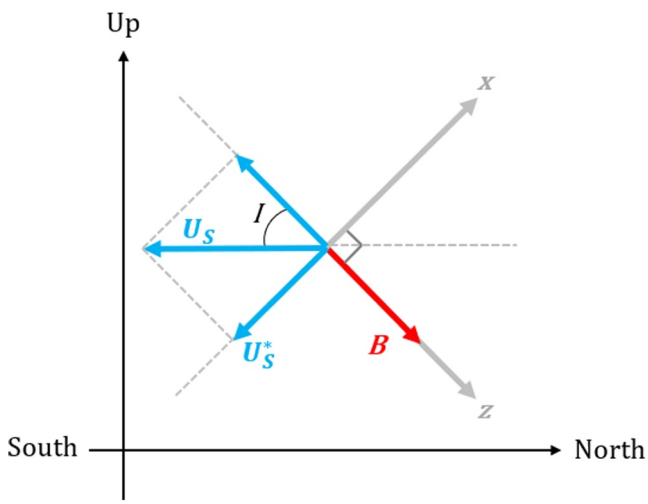

Figure 13. The projection of southward wind in *x*–*z* plane.

During storm time, the electric fields and winds undergo rapid changes. Perturbations exhibit varying responses to different background conditions at distinct developmental stages. Our simulation results indicate that small perturbations can develop into observable MSTIDs when the electric fields and winds are favorable for Perkins instability. Conversely, for the cases in which the effective electric fields are unfavorable, as demonstrated in Case 9, the amplitude of sinusoidal small perturbations in conductivity gradually decreased, but the sinusoidal shape remained intact.

Dramatic TID activities were observed during the 2018-08-25/26 magnetic storm event, MSTIDs were either intensified or well organized in the central US. Moreover, observed LSTIDs with large wavefronts elongated in the zonal direction were concurrent and adjacent to these MSTIDs. The temporal evolution and zonal propagation of MSTIDs during magnetic storms suggest that, they most likely seeded by the equatorward propagating LSTIDs with zonal wavefronts (Zhang et al., 2022). These initial perturbations leading to MSTIDs seem to exceed the 5% value in integrated conductivity used in Case 9. Simulations used also wind measurements at Millstone Hill, which is very far from the region where dominant MSTIDs were observed. Although simulations indicate that this particular southwestard wind pattern isn't favorable for Perkins instability growth, in the cases where there are already

significant initial disturbances, intensified stormtime electric fields can facilitate the perturbation to grow and winds can pull all the plasma features to move along southwestward via drag and dynamo action, despite they reduce the growth rate. Nevertheless, the contribution of neutral winds to the instability growth or suppression varies, depending on the wind direction. The timing of stormtime electric fields and winds may determine the time history of MSTIDs initiation, growth, and decay. The complication of strongly dynamic ionosphere-thermosphere coupling necessitates a sophisticated ionosphere-thermosphere model system to comprehensively account for the interplay between plasma and neutral components during the instability development.

Several important issues still need to be addressed when simulating MSTIDs in two-dimensional space. While the simulation results align well with the observed propagation direction and changes in perturbation development, the effect of conjugate ionosphere remains unknown, so is the E-F region coupling, although no Es-layer was identified in the storm cases examined by Zhang et al. (2022). Furthermore, the horizontal transport process along the magnetic field lines is anticipated to redistribute the accumulated plasma, which could possibly shed light on the late dissipation process of MSTIDs. Future investigations are desired to explore the inclusion of these factors in three-dimensional numerical models to provide more realistic MSTIDs simulations.

5. Conclusion

In this study, we have conducted a comprehensive investigation into the development of storm-time MSTIDs at midlatitude using a two-dimensional ionospheric electrodynamic model. The main results of this work are summarized as follows:

1. The results of our simulations of MSTIDs suggest that, in order to reproduce the electron density perturbations, it is essential to consider the storm induced horizontal gradient of the electron density at midlatitudes as initial ionospheric background. The polarization electric field plays a primary role in this nonlinear process.
2. MSTIDs exhibit faster growth rates at midlatitudes with lower magnetic inclination for a given electric field. This inference potentially explains the contrasting incidence of MSTIDs latitudinal preference for the same geographical longitude region.
3. The simulations further demonstrated that during storm time, the presence of enhanced electric fields aligned favorably for Perkins instability can drive the growth of MSTIDs in the F region, without invoking the Es instability. Specifically, the amplitude of density disturbance increased from 0% to 4.5% in about 1 hr under the influence of 30 mV/m applied electric field.

Data Availability Statement

Model results are available from the website http://doi.org/10.17605/OSF.IO/CNXRH (Wang et al., 2024). Solar wind and geomagnetic index data can be found from NASA OMNIWeb https://omniweb.gsfc.nasa.gov/form/omni_min.html. Millstone Hill Hi-Res FPI data can be downloaded from Madrigal: http://cedar.openmadrigal.org/single?isGlobal=on&categories=10&instruments=5360&years=2018&months=8&days=26.

Acknowledgments
This work was supported by the National Natural Science Foundation of China (42188101, 41831070), the Project of Stable Support for Youth Team in Basic Research Field, CAS (YSBR-018), and the International Partnership Program of Chinese Academy of Sciences (Grant number. 183311KYSB20200003), and the International Space Science Institute (ISSI) in Bern and Beijing, through ISSI International Team project #511 (Multi-Scale Magnetosphere-Ionosphere-Thermosphere Interaction). SRZ was supported by US NSF awards AGS-2033787, AGS-2149698, and AGS-1952737 and NRL Grant N00014-24-1-2122.

References

Blanc, M., & Richmond, A. D. (1980). The ionospheric disturbance dynamo. *Journal of Geophysical Research*, *85*(A4), 1669–1686. https://doi.org/10.1029/JA085iA04p01669

Chou, M.-Y., Lin, C. C. H., Huba, J. D., Lien, C.-P., Chen, C.-H., Yue, J., et al. (2018). Numerical modeling of the concentric gravity wave seeding of low-latitude nighttime medium-scale traveling ionospheric disturbances. *Geophysical Research Letters*, *45*(13), 6390–6399. https://doi.org/10.1029/2018GL077959

Cosgrove, R. B., Tsunoda, R. T., Fukao, S., & Yamamoto, M. (2004). Coupling of the Perkins instability and the sporadic E layer instability derived from physical arguments. *Journal of Geophysical Research*, *109*(A6), 1–11. https://doi.org/10.1029/2003JA010295

Duly, T. M., Chapagain, N. P., & Makela, J. J. (2013). Climatology of nighttime medium-scale traveling ionospheric disturbances (MSTIDs) in the Central Pacific and South American sectors. *Annals of Geophysics*, *31*(12), 2229–2237. https://doi.org/10.5194/angeo-31-2229-2013

Duly, T. M., Huba, J. D., & Makela, J. J. (2014). Self-consistent generation of MSTIDs within the SAMI3 numerical model. *Journal of Geophysical Research: Space Physics*, *119*(8), 6745–6757. https://doi.org/10.1002/2014JA020146

Erickson, P. J., Beroz, F., & Miskin, M. Z. (2011). Statistical characterization of the American sector subauroral polarization stream using incoherent scatter radar. *Journal of Geophysical Research*, *116*, A00J21. https://doi.org/10.1029/2010JA015738

Foster, J. C. (1993). Storm time plasma transport at middle and high latitudes. *Journal of Geophysical Research*, *98*(A2), 1675–1689. https://doi.org/10.1029/92JA02032

Foster, J. C., & Burke, W. J. (2002). Saps: A new categorization for sub-auroral electric fields. *Eos, Transactions American Geophysical Union*, *83*(36), 393–394. https://doi.org/10.1029/2002EO000289

Foster, J. C., Zou, S., Heelis, R. A., & Erickson, P. J. (2021). Ionospheric storm-enhanced density plumes. *Ionosphere Dynamics and Applications*, 115–126. https://doi.org/10.1002/9781119815617.ch6

Hamza, A. M. (1999). Perkins instability revisited. *Journal of Geophysical Research*, *104*(A10), 22567–22575. https://doi.org/10.1029/1999JA900307

Huang, C.-S. (2019). Long-lasting penetration electric fields during geomagnetic storms: Observations and mechanisms. *Journal of Geophysical Research: Space Physics*, *124*(11), 9640–9664. https://doi.org/10.1029/2019JA026793

Huang, C.-S., Foster, J. C., & Kelley, M. C. (2005). Long-duration penetration of the interplanetary electric field to the low-latitude ionosphere during the main phase of magnetic storms. *Journal of Geophysical Research*, *110*, A11309. https://doi.org/10.1029/2005JA011202

Jaggi, R. K., & Wolf, R. A. (1973). Self-consistent calculation of the motion of a sheet of ions in the magnetosphere. *Journal of Geophysical Research (1896-1977)*, *78*(16), 2852–2866. https://doi.org/10.1029/JA078i016p02852

Kelley, I. J. (2011). On the origin of mesoscale TIDs at midlatitudes. *Annals of Geophysics*, *29*(2), 361–366. https://doi.org/10.5194/angeo-29-361-2011

Kelley, I. J., Fejer, B. G., & Gonzales, C. A. (1979). An explanation for anomalous equatorial ionospheric electric fields associated with a northward turning of the interplanetary magnetic field. *Geophysical Research Letters*, *6*(4), 301–304. https://doi.org/10.1029/GL006i004p00301

Kelley, I. J., Kunduri, B. S. R., Baker, J. B. H., Ruohoniemi, J. M., & Shepherd, S. G. (2023). Storm time electrified MSTIDs observed over mid-latitude north America. *Journal of Geophysical Research: Space Physics*, *128*(3), e2022JA031115. https://doi.org/10.1029/2022JA031115

Kotake, N., Otsuka, Y., Ogawa, T., Tsugawa, T., & Saito, A. (2007). Statistical study of medium-scale traveling ionospheric disturbances observed with the GPS networks in Southern California. *Earth Planets and Space*, *59*(2), 95–102. https://doi.org/10.1186/BF03352681

Li, Z., Lei, J., & Zhang, B. (2021). Numerical considerations in the simulation of equatorial spread F. *Journal of Geophysical Research: Space Physics*, *126*(10), e2021JA029622. https://doi.org/10.1029/2021JA029622

Miller, C. A. (1996). *On gravity waves and the electrodynamics of the mid-latitude ionosphere*. Ph.D. thesis (p. 335). Cornell University.

Narayanan, V. L., Shiokawa, K., Otsuka, Y., & Neudegg, D. (2018). On the role of thermospheric winds and sporadic E layers in the formation and evolution of electrified MSTIDs in geomagnetic conjugate regions. *Journal of Geophysical Research: Space Physics*, *123*(8), 6957–6980. https://doi.org/10.1029/2018JA025261

Narayanan, V. L., Shiokawa, K., Otsuka, Y., & Saito, S. (2014). Airglow observations of nighttime medium-scale traveling ionospheric disturbances from Yonaguni: Statistical characteristics and low-latitude limit. *Journal of Geophysical Research: Space Physics*, *119*(11), 9268–9282. https://doi.org/10.1002/2014JA020368

Nishida, A. (1968). Coherence of geomagnetic DP 2 fluctuations with interplanetary magnetic variations. *Journal of Geophysical Research (1896-1977)*, *73*(17), 5549–5559. https://doi.org/10.1029/JA073i017p05549

Nishioka, M., Saito, A., & Tsugawa, T. (2009). Super-medium-scale traveling ionospheric disturbance observed at midlatitude during the geomagnetic storm on 10 November 2004. *Journal of Geophysical Research*, *114*, A07310. https://doi.org/10.1029/2008JA013581

Otsuka, Y., Shiokawa, K., Ogawa, T., & Wilkinson, P. (2004). Geomagnetic conjugate observations of medium-scale traveling ionospheric disturbances at midlatitude using all-sky airglow imagers. *Geophysical Research Letters*, *31*, L15803. https://doi.org/10.1029/2004GL020262

Otsuka, Y., Suzuki, K., Nakagawa, S., Nishioka, M., Shiokawa, K., & Tsugawa, T. (2013). GPS observations of medium-scale traveling ionospheric disturbances over Europe. *Annals of Geophysics*, *31*(2), 163–172. https://doi.org/10.5194/angeo-31-163-2013

Perkins, F. (1973). Spread F and ionospheric currents. *Journal of Geophysical Research (1896-1977)*, *78*(1), 218–226. https://doi.org/10.1029/JA078i001p00218

Shinbori, A., Otsuka, Y., Tsugawa, T., Nishioka, M., Kumamoto, A., Tsuchiya, F., et al. (2018). Temporal and spatial variations of storm time midlatitude ionospheric trough based on global GNSS-TEC and arase satellite observations. *Geophysical Research Letters*, *45*(15), 7362–7370. https://doi.org/10.1029/2018GL078723

Shiokawa, K., Ihara, C., Otsuka, Y., & Ogawa, T. (2003). Statistical study of nighttime medium-scale traveling ionospheric disturbances using midlatitude airglow images. *Journal of Geophysical Research*, *108*, 1052. https://doi.org/10.1029/2002JA009491

Shiokawa, K., Otsuka, Y., Ihara, C., Ogawa, T., & Rich, F. J. (2003). Ground and satellite observations of nighttime medium-scale traveling ionospheric disturbance at midlatitude. *Journal of Geophysical Research*, *108*, 1145. https://doi.org/10.1029/2002JA009639

Tsunoda, R. T. (2006). On the coupling of layer instabilities in the nighttime midlatitude ionosphere. *Journal of Geophysical Research*, *111*, A11304. https://doi.org/10.1029/2006JA011630

Tsunoda, R. T., & Cosgrove, R. B. (2001). Coupled electrodynamics in the nighttime midlatitude ionosphere. *Geophysical Research Letters*, *28*(22), 4171–4174. https://doi.org/10.1029/2001GL013245

Van Leer, B. (1977). Towards the ultimate conservative difference scheme III. Upstream-centered finite-difference schemes for ideal compressible flow. *Journal of Computational Physics*, *23*(3), 263–275. https://doi.org/10.1016/0021-9991(77)90094-8

Wang, X., Lei, J., Zhang, S.-R., Li, Z., Dang, T., Luan, X., & Dou, X. (2024). Simulation of nighttime medium-scale traveling ionospheric disturbances in the midlatitude ionosphere during stormtime:simulation data [Dataset]. *Open Science Framework*. https://doi.org/10.17605/OSF.IO/CNXRH

Yokoyama, T., & Hysell, D. L. (2010). A new midlatitude ionosphere electrodynamics coupling model (MIECO): Latitudinal dependence and propagation of medium-scale traveling ionospheric disturbances. *Geophysical Research Letters*, *37*, L08105. https://doi.org/10.1029/2010GL042598

Yokoyama, T., Hysell, D. L., Otsuka, Y., & Yamamoto, M. (2009). Three-dimensional simulation of the coupled Perkins and Es-layer instabilities in the nighttime midlatitude ionosphere. *Journal of Geophysical Research*, *114*, A03308. https://doi.org/10.1029/2008JA013789

Zhang, S.-R., Erickson, P. J., Coster, A. J., Rideout, W., Vierinen, J., Jonah, O., & Goncharenko, L. P. (2019). Subauroral and polar traveling ionospheric disturbances during the 7–9 September 2017 storms. *Space Weather*, *17*(12), 1748–1764. https://doi.org/10.1029/2019SW002325

Zhang, S.-R., Erickson, P. J., Zhang, Y., Wang, W., Huang, C., Coster, A. J., et al. (2017). Observations of ion-neutral coupling associated with strong electrodynamic disturbances during the 2015 St. Patrick's Day storm. *Journal of Geophysical Research: Space Physics*, *122*(1), 1314–1337. https://doi.org/10.1002/2016JA023307

Zhang, S.-R., Nishimura, Y., Erickson, P. J., Aa, E., Kil, H., Deng, Y., et al. (2022). Traveling ionospheric disturbances in the vicinity of storm-enhanced density at midlatitudes. *Journal of Geophysical Research: Space Physics*, *127*(8), e2022JA030429. https://doi.org/10.1029/2022JA030429

Zhou, Q. (2004). *A numerical investigation of the Perkins instability equations by the pseudo-spectral method*. Ph.D. thesis (p. 148). The Pennsylvania State University.

Zhou, Q., & Mathews, J. D. (2006). On the physical explanation of the Perkins instability. *Journal of Geophysical Research*, *111*, A12309. https://doi.org/10.1029/2006JA011696